

Fuel
Manuscript Draft

Manuscript Number: JFUE-D-16-00689

Title: Coal cleat reconstruction using microcomputed tomography imaging

Article Type: Original Research Paper

Keywords: Coal seam gas, X-ray microcomputed tomography, cleats, stochastic reconstruction, discrete fracture network

Abstract: Coal seam gas (CSG) is gaining global interest due to its natural abundance and environmental benefits in comparison to more traditional energy sources. However, due to its significant heterogeneity and complex porous structure, it is challenging to characterise and thus predict petrophysical properties. Moreover, the fracture network of coal poses a major challenge for direct numerical simulations on segmented images collected from X-ray microcomputed tomography (micro-CT). The segmentation of coal images is problematic and often results in misclassification of ~~col~~ features that subsequently causes numerical instabilities. Herein, an advanced image analysing method is developed to circumvent these issues. Coal ~~□~~CT data are utilised for the acquisition of structural parameters and then discrete fracture networks are built to reconstruct representative coal images. The modelling method mimics the cleat formation process and reproduces particular cleat network patterns. The reconstructed networks preserve the key attributes of coal, i.e. connectivity and cleat structure, while not being limited in terms of size and/or resolution. Furthermore, direct numerical simulations based on lattice Boltzmann method are performed on the cleat network realisations to evaluate coal permeability. We find that directional permeabilities result in different system scaling effects because of the dependence on the underlying structure of the cleat network. The developed method facilitates evaluation of the relationship between coal cleat structure and resulting flow properties, which are steps forward in the evaluation of coal petrophysical properties at the core-plug scale.

Coal cleat reconstruction using microcomputed tomography imaging

Yu Jing, Ryan T. Armstrong, Hamed Lamei Ramandi and Peyman Mostaghimi

School of Petroleum Engineering, The University of New South Wales, NSW 2052, Sydney, Australia

ABSTRACT

Coal seam gas (CSG) is gaining global interest due to its natural abundance and environmental benefits in comparison to more traditional energy sources. However, due to its significant heterogeneity and complex porous structure, it is challenging to characterise and thus predict petrophysical properties. Moreover, the fracture network of coal poses a major challenge for direct numerical simulations on segmented images collected from X-ray microcomputed tomography (μ CT). The segmentation of coal images is problematic and often results in misclassification of coal features that subsequently causes numerical instabilities. Herein, an advanced image analysing method is developed to circumvent these issues. Coal μ CT data are utilised for the acquisition of structural parameters and then discrete fracture networks are built to reconstruct representative coal images. The modelling method mimics the cleat formation process and reproduces particular cleat network patterns. The reconstructed networks preserve the key attributes of coal, i.e. connectivity and cleat structure, while not being limited in terms of size and/or resolution. Furthermore, direct numerical simulations based on lattice Boltzmann method are performed on the cleat network realisations to evaluate coal permeability. We find that directional permeabilities result in different system scaling effects because of the dependence on the underlying structure of the cleat network. The developed method facilitates evaluation of the relationship between coal cleat structure and resulting flow properties, which are steps forward in the evaluation of coal petrophysical properties at the core-plug scale.

Keywords: Coal seam gas, X-ray microcomputed tomography, cleats, stochastic reconstruction, discrete fracture network

1 INTRODUCTION

Coal seam gas (CSG), also known as coal bed methane (CBM), is a form of unconventional natural gas extracted from coal reservoirs. In the past, methane was vented during mining operations for safety concerns, but now it makes a significant contribution to powering both industry and households (Hamawand et al. 2013, Rodrigues et al. 2014). As a result, the study of coal structure is considered crucial, because CSG production is mainly controlled by coal permeability (Gamson et al. 1993, Pattison et al. 1996), which in turn is related to the underlying fracture network, called ‘cleats’. Coal cleats theoretically occur in two main sets of sub-parallel fractures, “face cleats” and orthogonal “butt cleats” as demonstrated in Figure 1 (Scholtès et al. 2011). In most circumstances, face cleats are formed first during coalification, whereas butt cleats occur later and terminate at face cleats, resulting from the relaxation of the original stress field (Scholtès et al. 2011, Gao et al. 2014). In other words, for an organised cleat set, the connectivity pattern mostly presents “T-junctions” between face cleats and butt cleats. Generally, the 3D description of cleats includes spacing, geometry, orientation, aperture size, connectivity, degree of mineralisation and topology, all of which can influence methane production (Laubach et al. 1998).

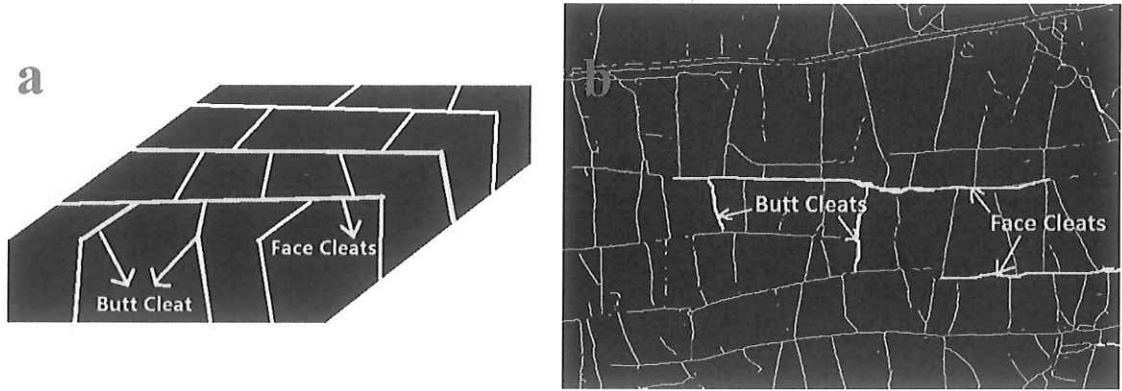


Figure 1: An illustration of face cleats and butt cleats in a conceptual model (a) and real cleat system (b). Face cleats are orthogonal to butt cleats, and butt cleats terminate at face cleats.

OR MISSING
SONEN(?)

(1) equivalent

MISSING PAGE ?

continuum model (ECM) (Svensson 2001, Botros et al. 2008, Parashar and Reeves 2011); (2) dual-continuum model (DCM) (Warren and Root 1963, Kazemi et al. 1976); and (3) discrete fracture network model (DFN) (Dershowitz and

SC PE Einstein 1988, Cacas et al. 1990). ECM is the most simplified model where a number of regions are defined in which physical properties such as transmissibility and storage are uniform. These physical properties are computed from a fracture network realisation and then volume averaged for the total rock size, including matrix and fractures (Hsieh et al. 1985). The DCM, also known as the dual-porosity model, originates from the study of Barenblatt et al. (1960) and was introduced by Warren and Root (1963). This model is comprised of primary porosity and secondary porosity. Flow can occur between the primary and secondary porosities through an exchange term, but no flow is considered in the primary porosity. Later, the model was developed to account for flow in both domains, i.e. the dual permeability model (Blaskovich et al. 1983, Hill and Thomas 1985). Both ECM and DCM are prevalent in industry due to their simplicity and computing efficiency. They are however extremely simplified representations of complex fracture networks and inherent non-physical abstractions often make them inadequate for the accurate determination of flow properties in fractured reservoirs.

In contrast to continuum models, DFN assumes that fluid transport in fractured rock is dominated by a number of unique pathways formed by discrete fractures. Therefore, instead of average or effective medium properties, DFN describes the geometry and attributes of discrete fractures explicitly (Dershowitz et al. 2004). Thus, it is the most accurate approach for modelling fracture systems (Gong 2007). Advantages of DFN modelling are summarised as follows: (1) It can account for physical geological parameters, such as fracture orientation, length, aperture size and depth; (2) it can be upscaled to a dual medium model, which can be solved using conventional computational methods, such as finite difference; (3) it can assess larger scale connectivity, such as faults and large fractures; and (4) it can quantify the uncertainty and heterogeneity of porosity and permeability using stochastic methods (Marie Lefranc

2012). DFN also suffers some drawbacks. For instance, it requires more computational time in comparison to ECM and DCM (Long and Witherspoon 1985, Parashar and Reeves 2011) and mesh generation for arbitrary fracture networks can be complicated and challenging (Gong 2007).

The first use of DFN models for flow in fractured porous media was in the early 1980s and these models consisted of discrete planes in 3D or line segments in 2D. Baecher et al. (1977) established a DFN model based on the statistical description of rocks, in which fractures were circular disks, based on the findings of Robertson (1970). They assigned random centre points following Poisson distribution, lognormal distributed radii and weighted frequency distributed orientations to the disks, while neglecting aperture size distribution. Afterwards, Cacas et al. (1990) further developed DFN modelling by applying the Fisher von Mises distribution on fracture orientation and classifying the orientation into different families. In addition, they used a lognormal distribution to characterise fracture aperture sizes. Cacas's method of building DFN models is still widely used, while the distributions may vary according to the observed field data. Apart from conventional fractured rocks, DFN modelling is also feasible for coal reservoirs (Deisman et al. 2010, Scholtès et al. 2011, Gao et al. 2014, Yang et al. 2014, Lorig et al. 2015). Nevertheless, most of the coal studies simply generate DFN models stochastically based on statistical descriptions of the cleat network and thus disregard the underlying connectivity of face and butt cleats. Only a limited number of studies consider the potential spatial organisation of the cleat system. For example, Gao et al. (2014) built a DFN model for coal cleat systems, which consists of three orthogonal discontinuity sections: (1) bedding planes; (2) face cleats; and (3) butt cleat. This DFN model seems to describe coal rather well however the independent orientation statistics of the face and butt cleats were not included. Therefore, they failed to reproduce the characteristic "T-junctions" that are common in fractured coal seams (Maillot et al. 2014). Herein, a novel DFN model is designed specifically for coal cleat networks that considers the independent distribution statistics of face and butt cleats and then generates networks in a way that mimics the geological formation of the cleat network.

DFN models can be constructed for a large range of length scales, ranging from field scale (> 1 km) to core plug scale (1-10 cm). Cleats on different scales require different approaches to obtain the necessary statistical data for DFN reconstruction. For instance, cleat network reconstruction on larger scales (m to km) combines seismic, well logging, outcrop analysis, and coring data. But such quantitative field data are not always available and often extremely expensive. In this paper, we characterise fractures at the core plug scale using a non-destructive imaging technology called X-ray micro-computed tomography (μ CT). This technique has the capability of detecting cleats at the micrometre length scale in core plugs that are many centimetres in diameter. There are several relevant works on the

application of μ CT scanning for coal characterisation and modelling. Mazumder et al. (2006) applied μ CT to analyse cleat spacing, aperture sizes and orientation. However, they lacked a comprehensive way to determine cleat spacing statistics. More specifically, fractures of non-desirable directions were suppressed manually, then a set of parallel lines perpendicular to a pre-defined direction were added to the image, finally only line segments that were connection from one cleat to another were measured. This manual measurement approach is not practical for hundreds or thousands of images. Besides, Mazumder et al. (2006) never applied there generated networks to coal samples nor the modelling of transport properties. Bossie-Codreanu et al. (2004) further utilised these distributions for the measurement of petrophysical properties. They stochastically generated DFN models according to cleat attribute distributions, and then a number of subsamples were selected in the model. For each subsample, permeability was calculated by computing the flow rates of every node. Together with the corresponding porosity values, they plotted the resulting permeability versus porosity relationship. But their DFN models were based on unrealistic assumptions and simplifications. In particular, all of the generated fractures crossed the entire model without considering fracture length variety, which creates a highly conductive model. Most recently, Voorn et al. (2014) also conducted quantitative μ CT imaging and analysis for DFN modelling, but the sample was not coal. They compared the results of porosity determined by μ CT, Scanning Electron Microscopy (SEM) and laboratory methods, as well as the numerical and experimental permeability. Nevertheless, they did not include fracture spacing and length, which are essential parameters for coal cleat characterisation. In addition, their model for permeability calculation was derived by Gueguen and Dienes (1989), where permeability is simply a function of porosity, average aperture size and a factor depicting the fraction of connected fractures, rather than direct numerical simulation.

As discussed there are many challenges with the characterisation of cleats from μ CT images and the subsequent reconstruction of cleat networks using DFN approaches. The main unresolved issues can be summarised as the following: (1) independent cleat property statistic for face and butt cleats have not been considered; (2) the length of cleats is often disregarded; (3) cleat spacing measurements are commonly lacking; (4) DFN reconstruction often disregards the underlying cleat structure; (5) when solving for the permeability over-simplified analytical methods are often utilised; and (6) cleat connectivity is often disregarded. This paper discusses the development of a novel framework for cleat characterisation while offering solutions to these challenges. In addition, we do not utilise DFN models in the traditional approach where Darcy formulations are used to solve for flow. Rather we voxelise the discrete fracture network and thus create a model domain suitable for direct numerical simulation using the lattice Boltzmann method. The focus is on the core-scale characterisation of coal and the reconstruction of cleat networks with DFN provides a solution to many of the difficulties with the direct simulation of flow on micro-CT images. For

] obj

example, micro-CT images often have bottleneck features caused by resolution limitations and/or image segmentation error. Such features are a major challenge for numerical solvers due to the numerical instabilities that results from limited voxel resolution. Herein, we circumvent this issue by using the DFN approach for the reconstruction of digital coal images at the pore-plug scale that have well defined fracture apertures.

2 METHODOLOGY

The first step for coal cleat characterisation is acquiring the μ CT image in which the details are described by Ramandi et al. (2016). After quantitative μ CT imaging and analysis, statistics of cleat geometric attributes are acquired. Based on the statistical data, stochastic models are generated using the Monte Carlo method (Chen et al. 2008). For each realisation, the model is voxelised and then flow is numerically simulated to calculate permeability. Figure 2 provides an overview of our approach and in the following section the details for each step will be discussed.

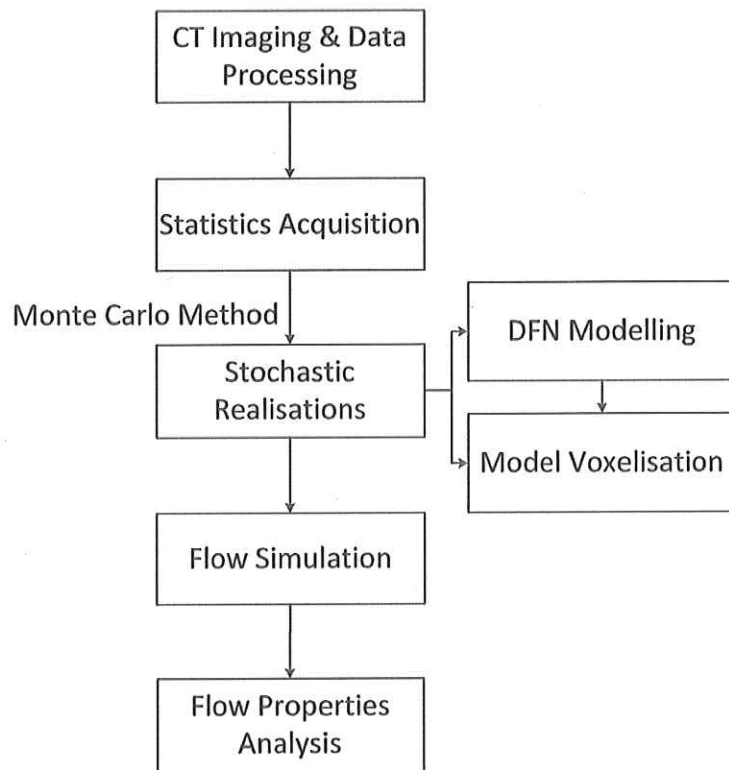


Figure 2: Overview of the methodology. Statistics of cleat attributes, measured from the segmented μ CT images, are input to reconstruction of the DFN models, giving a set of stochastic realisations with Monte Carlo method. For each realisation, flow properties are simulated, including connectivity, permeability and porosity.

2.1 Statistics Acquisition

2.1.1 Equipment and Data Processing

We use the helical scanning micro-CT instrument developed at the Australian National University (Sheppard et al. 2014). In the helical scanning technique a series of radiographs, i.e. projections, are collected around the object at different viewing angles while the sample moves according to a helical trajectory. To generate a 3D spatial

representation of the specimen (tomogram), the projections are reconstructed using an algorithm based on the Katsevich (2002) inversion formula for a helix trajectory. The sample is imaged in both dry and wet (saturated with an X-ray attenuating fluid) conditions. The X-ray attenuating fluid is a mixture of 1.5 molar Sodium Iodide (NaI) and 1.0 molar Potassium Chloride (KCl). The sample is initially saturated under vacuum, and then to ensure that all fluid-accessible pores and fractures are saturated, the fluid is injected at ~670 bar. X-ray attenuating fluid reveals micro-sized pores and fractures which are not readily visible with conventional techniques (Ramandi et al. 2016). A 3-mm aluminium filter is used to minimize beam-hardening artefacts by attenuating soft X-rays at the source.

Registration techniques developed by Latham et al. (2008) are used for registering the dry and wet images. Then, the registered wet and dry images are subtracted to provide a difference image in which the contrast between different features is high enough for image segmentation (Figure 3). Prior to segmentation, it is required to remove noise from the images while preserving the coal features and boundary regions. We apply an anisotropic diffusion (AD) filter for de-noising that preserves fracture edges while enhancing the signal-to-noise ratio of the data (Gonzales and Woods 1987). After the AD filter, an unsharp mask (UM) filter is applied for sharpening edges without excessively intensifying the noise (Sheppard et al. 2004). For segmenting of the grey-scale image into distinct phases, e.g. minerals, macerals and fractures, the converging active contours (CAC) method is utilised (Sheppard et al. (2004)). CAC is based on a combination of the watershed method (Vincent and Soille 1991) and active contour methods (Caselles et al. 1997) in which the segmentation begins with choosing lower and upper threshold values. Voxels with values less than the lower threshold are classified as voids and the voxels with values above the upper threshold are classified as solids. The values between the lower and upper thresholds are the unclassified region. CAC expands the classified regions towards each other, within the unclassified region, to set the boundary at the locations where two contours converge. The local gradient and the distance of the local voxel value to the mean voxel value of its corresponding phase defines the speed at which the boundaries expand (Schlüter et al. 2014). Three successive CACs are applied on the filtered 3D difference image to segment it into four phases: (1) cleat network, (2) sub-resolution porosity, (3) coal macerals (organic materials), and (4) mineral phase (inorganic minerals). More details on image acquisition and segmentation of coal can be found in Ramandi et al. (2016). The segmented cleat network is used for the generation of the statistical data.

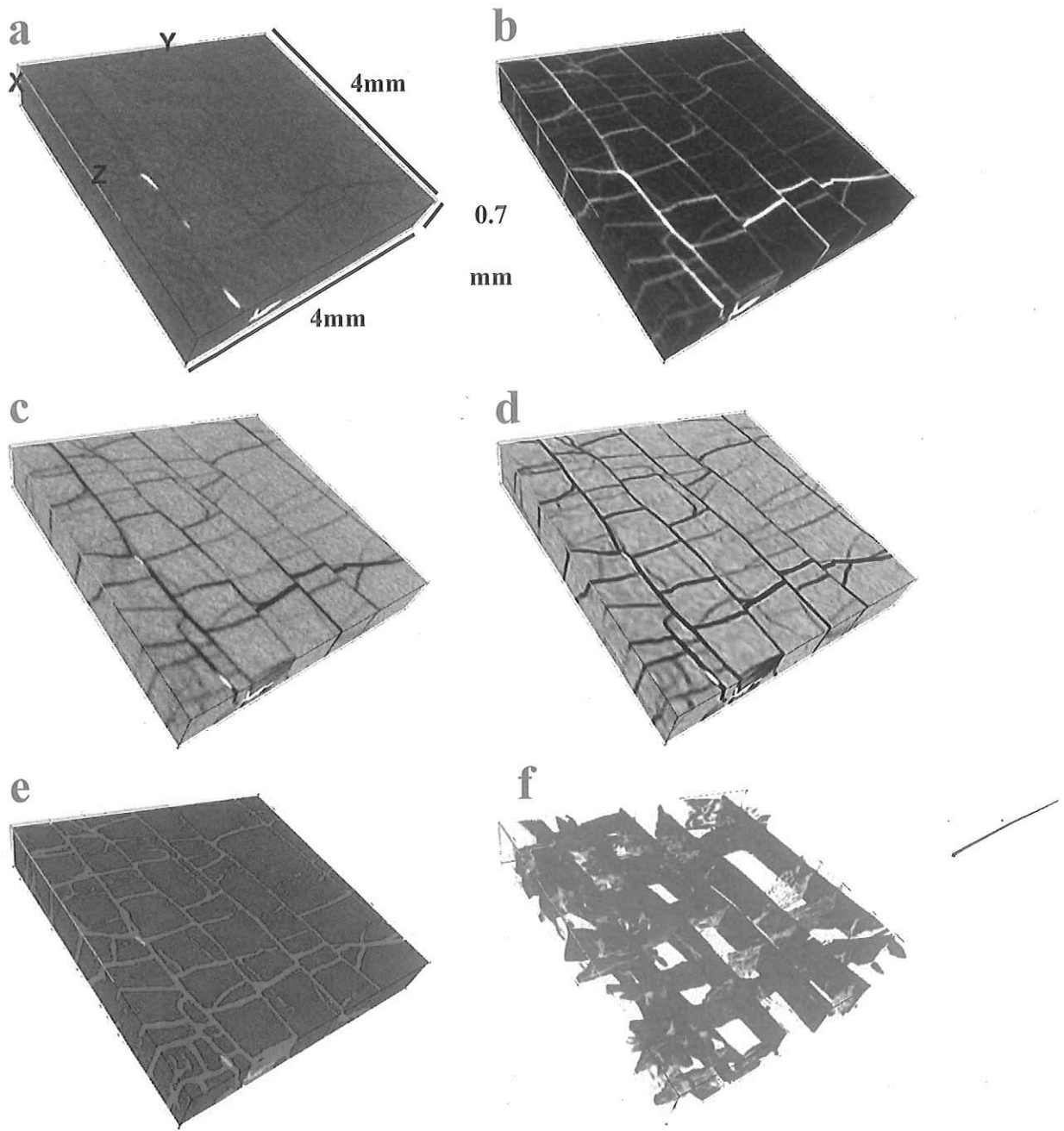


Figure 3: 3D visualisation of coal cleat structure: (a) the dry image; (b) the wet image; (c) the difference image before enhancement; (d) difference map after applying AD and UM filters; (e) segmented image (red: fracture network, grey: macerals, yellow: minerals); and (f) fracture network.

2.1.2 Cleat Type Classification

Cleat type classification is performed to distinguish between face and butt cleats. This is essential for the subsequent image analysis, especially in terms of spacing and length measurements since face and butt cleats have different property statistics (Laubach et al. 1998). After segmentation, cleats are first skeletonised with a thinning algorithm, reducing the cleats to one-voxel wide features (Lee et al. 1994). On the 2D skeletonised slice, each pixel representing a fracture is tagged with 8 neighbours. We spin the image such that the majority of the cleats are placed horizontally

and then based on the direction in which the tagged cleat pixel extends the cleats are classified into: (1) horizontally-oriented, (2) vertically-oriented and (3) others. Since the tested coal sample in this paper is well fractured and has a regular cleat pattern, less than 5% of cleats are classified as (3) others, thus we assume that cleats other than face or butt cleats have an insignificant effects on the overall permeability and are removed to simplify the model. Therefore, as displayed in Figure 4, this procedure splits the segmented μ CT image into two sets: (1) face cleats and (2) butt cleats, which is used to extract independent statistics.

However, the classification algorithm shortens the length of the cleats, especially for face cleats (Figure 4). Therefore, the classification algorithm may result in disconnected and short cleat segments rather than continuous cleats, which influences the cleat length measurements and sequentially influences the generated DFN model. However, to overcome this issue, a special fracture generation sequence is developed as described in the DFN reconstruction section.

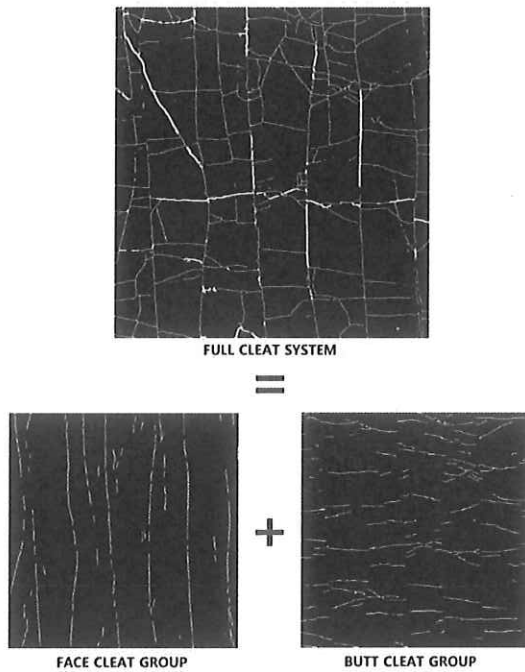


Figure 4: An example of classifying the cleat system into face cleat and butt cleat groups based on orientations. The cleats other than face and butt ones are filtered out in this case. Due to the limitation of the classification process, extend face cleats are broken into segments. But this is solved in the DFN reconstruction section.

2.1.3 Analysis of μ CT Images

Once the images are divided into face and butt cleats, the independent distributions of cleat orientation, length, spacing, aperture size, and intensity are measured. These measurements are rather robust since only the statistical

distributions of these properties are required. Therefore, the segmented data can have a considerable amount of noise, i.e. the segmentation of coal cleats does not require perfection. Rather only the majority of cleats need to be identified.

1. Orientation

ref other work but did not explain how it does do!

Common methods for measuring fracture orientation includes the work of Mazumder et al. (2006) and Wolf et al. (2008). In addition, Voorn et al. (2014) presented another way of measuring orientations on 3D networks by using the eigenvectors and eigenvalues to represent the normal direction of the fracture plane at each voxel. For our case, based on structure tensors, which are matrix representatives of partial derivatives, the local orientations and isotropic properties of every pixel of the image is evaluated and the largest eigenvector of the tensor corresponds to the orientation (Jahne 1993, Bigun et al. 2004).

2. Length

Commonly in the literature, length is implicitly included in the orientation measurement by presenting the accumulated lengths versus the corresponding orientation (Bossie-Codreanu et al. 2004, Mazumder et al. 2006). However, length is highly related to cleat type. Usually, face cleats are more thorough-going and extensive, while butt cleats often terminate at face cleats (Seidle 2011). Thus, face cleats exhibit larger lengths compared to butt cleats, and it is necessary to apply the length measurement procedure on face and butt cleats separately. To measure lengths, we first measure the area of every cleat expressed by the number of pixels, which represents the length in the skeletonised structure, and then remove short isolated cleats according to a user-defined length threshold. The threshold is determined by examining the images after skeletisation, extremely short and isolate cleat segments resulting from improper segmentation are regarded as noise and thus are removed.

3. Spacing

Mazumder et al. (2006) developed an algorithm to measure cleat spacing such that a grid of parallel lines were added to the μ CT image with the orientation perpendicular to the cleat angle. Then, the lengths of parallel line segments were measured, representing the spacing statistic data. However, manual editing was required in this part, especially for some disconnected, short or undesirable oriented cleats. In our framework, owing to the previous step of the orientation filtration, no manual aid is needed. Spacing of face cleats and butt cleats are measured separately. The spacing is measured by determining the distance between the Cartesian voxel positions of adjacent cleats.

4. Aperture

There are many methods for measuring fracture aperture sizes, e.g. [Johns et al. 1993, Vandersteen et al. 2003, Muralidharan et al. 2004]. When scanning across a μ CT image, the CT number at an aperture shows a reduction. This obvious dip in the profile of the CT number indicates the existence of fractures. Two main parameters describing the dip are peak height (PH) and missing attenuation (MA) (Ketcham et al. 2010). By plotting the relationship between PH or MA and the corresponding aperture size a calibration curve can be obtained (Mostaghimi et al. 2015a). In this way, aperture sizes can be estimated from the CT number profile across a fracture. In addition, aperture can also be measured directly from μ CT scans (Voorn et al. 2014) by means of placing 3D spheres inside fractures. The diameter of the largest sphere that fits inside can be regarded as the aperture of the corresponding fracture (Dougherty and Kunzelmann 2007). However, the direct measuring method is significantly influenced by the μ CT image resolution and segmentation errors. A new technique is developed for more accurate aperture measurement in digital images. Together with dry and wet (saturated) imaging of the sample, high-resolution SEM images from the sample surface are obtained and registered to the digital images. Then plotting attenuation coefficients against the measured aperture sizes in the corresponding SEM images generates a calibration curve. In this way, apertures that are smaller than the resolution can be calculated. To be exact, according to the calibration curve, at each fracture midpoint attenuation coefficient, its corresponding aperture size can be calculated from the calibration curve. Lastly, a new image is generated with higher resolution, which is acquired from the μ CT image but has the precise aperture sizes assigned based on the high-resolution SEM images (Mostaghimi et al. 2015a). The aperture measurement is not conducted on different cleat families separately, because the cleat family classification is based on skeletised cleats, which do not have opening widths. So the aperture statistics are for both cleat types and do not consider face and butt cleats independently.

5. Intensity

Three dimensional intensity ($P_{31}[\text{m}^{-1}]$), the total fracture surface area per sample volume (Dershowitz et al. 2000) is calculated. For voxel-based binary images, after skeletisation, fracture intensity can be estimated by the following equation

$$P_{31} = \frac{N_f}{N_t \times a} \quad (1)$$

where N_f is the number of fracture-labelled voxels, N_t is the total number of voxels, and a is the length of a voxel.

2.2 DFN RECONSTRUCTION

As mentioned prior, coal cleat networks present unique spatial distributions compared to other naturally fractured rocks. For an organised cleat set, the connectivity pattern will mostly present “T-junctions” between face cleats and butt cleats. But for a common DFN model, its fracture parameters, e.g. density, length, and orientation, are independently drawn from statistical distributions, known as the Poisson model (PM). This is not applicable for coal samples (Maillet et al. 2014), since PM approaches do not consider the connectivity pattern of the fractured network, even though the probability distributions of properties are correct. Thus, in this study, a novel DFN reconstruction method is developed by integrating fracture mechanics into the probabilistic framework. The cleat reconstruction procedure mimics the natural process of cleat formation, which involves generating face cleats first based on the measured spacing and then butt cleats are produced randomly between the face cleats to form “T-junctions”. A cleat, especially a long face cleat, might be seen to break into several cleat segments on binary images, due to cleat family classification issues. To overcome this issue, the spaced face cleats are generated first, and then we add the shorter face cleat segments along their extending trends, until the desired accumulated length of face cleats is reached. In this model, we assume that each fracture is a smooth, planar rectangular surface. Periodic boundary conditions are applied in all directions to eliminate surface effects. The overall procedure, as demonstrated in Figure 5, is explained as:

1. Determine the centre point positions of major face cleats on first layer based on the spacing statistics data of face cleats.
2. Assign the largest lengths, from the length distribution data, to above the centre points and rotate them randomly according to the face cleat orientation distribution.
3. Extend the major face cleats by adding more cleats until the desired accumulated length is satisfied.
4. Locate randomly the end points of butt cleats along the generated face cleats with measured spacing based on the butt cleats spacing data. The end points are then intersected with the face cleats.
5. Allocate aperture sizes to all of the generated cleats based on the aperture size distribution data, completing the 2D DFN layer as displayed in Figure 7b.
6. Measure the cleat orientations in XZ and YZ plane, calculating the coordinates of the centre points of the next layer (the layer distance depends on the desired resolution in Z direction). Then, repeating steps 1 through 5, providing the next 2D DFN layer.
7. Repeat the above steps until a 3D model is constructed with the desired dimensions.

(*)

An example realisation is provided in Figure 6. It is clear that the realisation captures the main structural features of the original coal cleat image. The face cleats are through going and the butt cleats terminate at face cleats creating characteristic "T-junctions". In addition the spacing, connectivity and orientation of the generated cleat network resembles the original cleat image rather well.

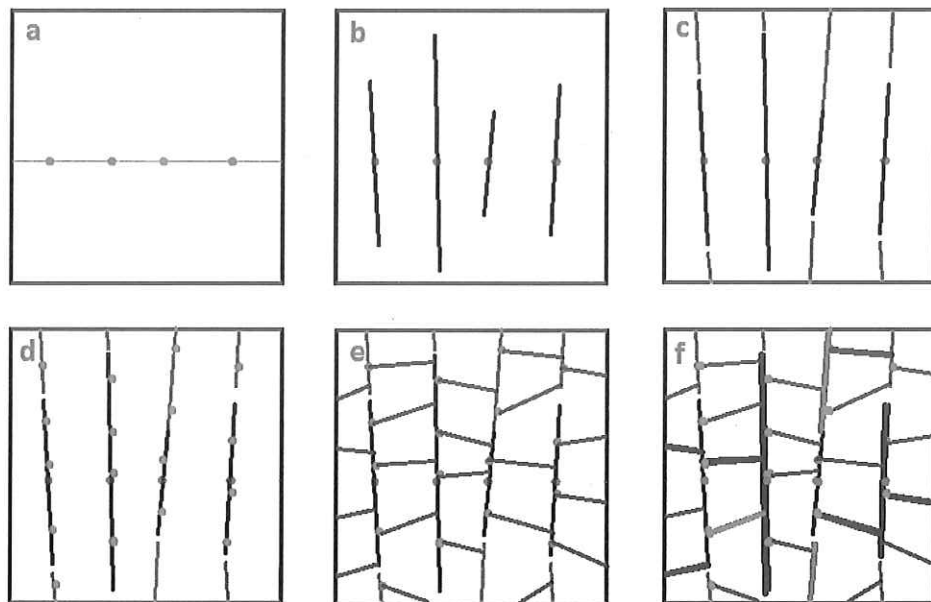


Figure 5: DFN modelling workflow in XY plane: (a) randomly spaced centre point positions of face; (b) assign random length and orientations; (c) extend these face cleats; (d) green points are butt cleat end points; (e) stochastic oriented butt cleats terminated by face cleats; (f) applying apertures.

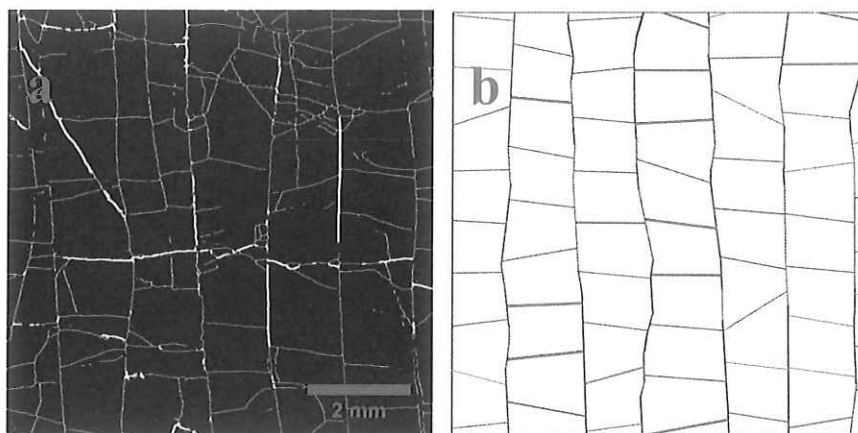


Figure 6: Top view of original coal (a) and its stochastic DFN model (b). As can be seen, DFN (b) represents the main features of original sample (a). This approach is specifically important when the original images are noisy, poorly segmented, and/or has low resolution.

(*)

How do you "measure" / "calculate" similarities between original scan and stochastic DFN model?

2.3 Calculation of Connectivity

The connectivity of fractures is a key factor that influences fluid flow in cleat networks (Alghalandis et al. 2011). In reality, the connectivity of real fractured medium is difficult to estimate and to use as conditioning data (Bonneau et al. 2013). It is common for discrete fracture models to regenerate non-conductive fracture networks and thus underestimate fracture connectivity, even for cases with high fracture density (Alghalandis et al. 2011, Bonneau et al. 2013). The DFN model proposed in this paper however mimicks the natural process through which cleats are formed, i.e. face cleats followed by butt cleats, and thereby the reconstruction preserves the connectivity of the original image. Robinson (1983) proposed that the fracture network connectivity could be accurately quantified by the average number of fracture intersections per fracture. However, more recently Rodrigues et al. (2014) proposed that connectivity can be defined as the total length of intersection lines per unit sample volume in 3D (Rodrigues et al. 2014). This definition is used in our study since all of the intersection points have already been calculated during the DFN construction and thus this measurement is easily obtainable with practical units whereas the previous connectivity definition by Robinson (1983) results in abstract units.

2.4 Voxelisation of DFN Models

Prior to numerical simulation, discretisation is required to convert the continuous geometry to discrete elements. Compared to conventional discretisation approaches (Yuen et al. 1991, Vohralík et al. 2007, Erhel et al. 2009), a process named voxelisation is utilised to provide binary files that have the same format as the segmented μ CT images. Specifically, equal cubic grids are overlayed onto the DFN model, and grid cells with fractures are set as 1, otherwise grid cells are 0. The convenience of this approach is that direct numerical simulations can be performed on the generated fracture network, i.e. single phase and two phase flow and/or mass transfer. This approach also avoids many of the common problems of direct numerical simulation on μ CT images of coal: (1) limited image resolution where cleats are not entirely segmented; (2) isolated voxel islands from imaging noise; and (3) bottle-necks of single pixel resolution due to segmentation error. Alternatively, generated DFN models have well-defined cleat intersections with well-resolved fractures resulting in a model domain that is well suited for direct numerical simulation.

PE
SC { Certainly, the voxelisation process determines the resolution of the resulted binary image, which is the grid number placed onto the model. In this work, the resolution is identical to the resolution of the μ CT image, however there are approaches of upsampling of the data to increase the grid resolution within the highly constricted fracture apertures (Mostaghimi et al. 2015a).

2.5 Calculation of Petrophysical Properties

2.5.1 Porosity

After voxelisation, the bulk porosity is determined by dividing the amount of fracture-identified voxels by the total number of voxels. The calculated porosity is highly dependent on the model resolution. For instance, low resolution means larger voxel size, inducing fractures with wider openings. The porosity of the initial μ CT data is calculated using the same method, while it is also affected by initial image quality. The image resolution of 16 micrometre has been shown to be sufficient to capture the porosity of coal accurately with less than 15% error between image-based porosity and experimentally measured porosity (Ramandi et al. 2016).

2.5.2 Permeability

There are several methods to calculate the effective properties of DFN models. One approach is developed by Oda (1985), in which the permeability tensor is derived by computing steady-state flux through parallel slits and then solving for permeability using Darcy's law. With this approach, the entire fractures in the grid are represented by fracture tensors calculated by summing up the normal components of the fracture. This method is fast but not accurate enough (Oda 1985, Pan et al. 2010, Elmo et al. 2014, Maffucci et al. 2015). Other methods are flow-based, one of which uses finite element method (FEM) to run the flow simulation (van der Most 2008, Correia et al. 2011, Lang et al. 2014). This approach requires meshing the model domain, which is comprised of an unstructured tetrahedral mesh representing the matrix, and a triangulated mesh representing the fracture surfaces. This method can provide more accurate results but mesh generation is a challenging and time consuming (Mostaghimi and Mahani 2010, Marie Lefranc 2012, Mostaghimi et al. 2014, Mostaghimi et al. 2015b).

} what is the relationship here?

Herein, the lattice Boltzmann method is utilised, which is based on a three-dimensional lattice with nineteen possible momenta components, D3Q19 (Arns et al. 2005, Norouzi Apourvari and Arns 2015). Fluid flow is simulated by solving the discrete Boltzmann equation,

$$f_i(\vec{x} + \vec{e}_i \delta_t, t + \delta_t) - f_i(\vec{x}, t) = \Omega_i(\vec{x}, t) \quad (2)$$

$$\left\{ \begin{array}{l} \vec{x} \\ \vec{e}_i \\ \delta_t \\ t \end{array} \right\} \left\{ ? \right\}$$

where f_i is the particle distribution function in the i -direction, \vec{e}_i is the microscopic velocity, and Ω is the collision operator. According to the Bhatnager-Gross-Krook (BGK) model, the collision operator is expanded as,

$$\Omega_i(\vec{x}, t) = -\frac{f_i(\vec{x}, t) - f_i^{eq}(\vec{x}, t)}{\tau} \quad (3)$$

where f_i^{eq} is the local equilibrium state and τ is the relaxation time. The macroscopic fluid flow quantities, density and velocity, are then calculated using $\rho = \sum_i f_i$ and $\vec{u} = \frac{1}{\rho} \sum_i (f_i \vec{e}_i)$, respectively. The bounce-back rule (Martys and Chen 1996) is applied on the solid-fluid interfaces, acting as no-flow boundary conditions. The pressure gradient acting on the fluid is simulated by a body force and mirror image boundary conditions are applied on the plane perpendicular to the flow direction. Lattice Boltzmann is proven to be able to reproduce the incompressible Newtonian Navier-Stokes equation with kinematic viscosity of $\frac{1}{3} \left(\tau - \frac{1}{2} \right)$ (Chen et al. 1992).

3 RESULTS AND ANALYSIS

3.1 Cleat Attribute Measurements

A bright coal sample is chosen from Moura mine of Bowen Basin, Australia for μ CT scanning. The sample is a medium volatile bituminous coal, with a vitrinite reflectance of 1.15%. More details about the sample specification and geological formation have been reported in Ramandi et al. (2016). To reconstruct the cleat network, a 3D domain is cropped with the size of $960 \times 960 \times 170$, and a voxel size of $4.1 \mu\text{m}$. The segmented μ CT images (Figure 7) indicate that the sample has a well-developed cleat network, representing the classical face and butt cleats. It is also evident that the segmented image has a considerable amount of noise, isolated voxels and under-resolved cleats. However, as will be demonstrated, this has little to no effect on the generated DFN realisations.

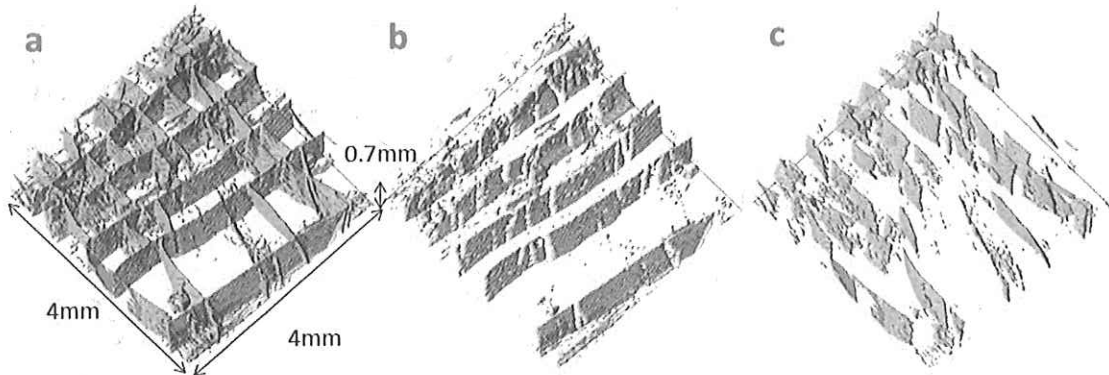


Figure 7: 3D CT image: (a) the whole cleat network; (b) filtered face cleats; and (c) filtered butt cleats. The face and butt cleats are classified and studied independently.

Figure 8 and Table 1 summarise the measured distributions of cleat spacing, orientation and length. The orientations are gathered around 0 degree and ± 90 degree, which represents the orthogonal face and butt cleats. The length histograms show a power law distribution and spacing distributions of face and butt cleats have similar mean values, indicating face and butt cleats are evenly spaced. However, butt cleats show a wider range in spacing distribution, and

similar trends are observed for azimuth data. Therefore, butt cleats are more irregular in terms of spacing and orientation compared to face cleats, which is likely to have a strong influence on the directional flow properties of coal.

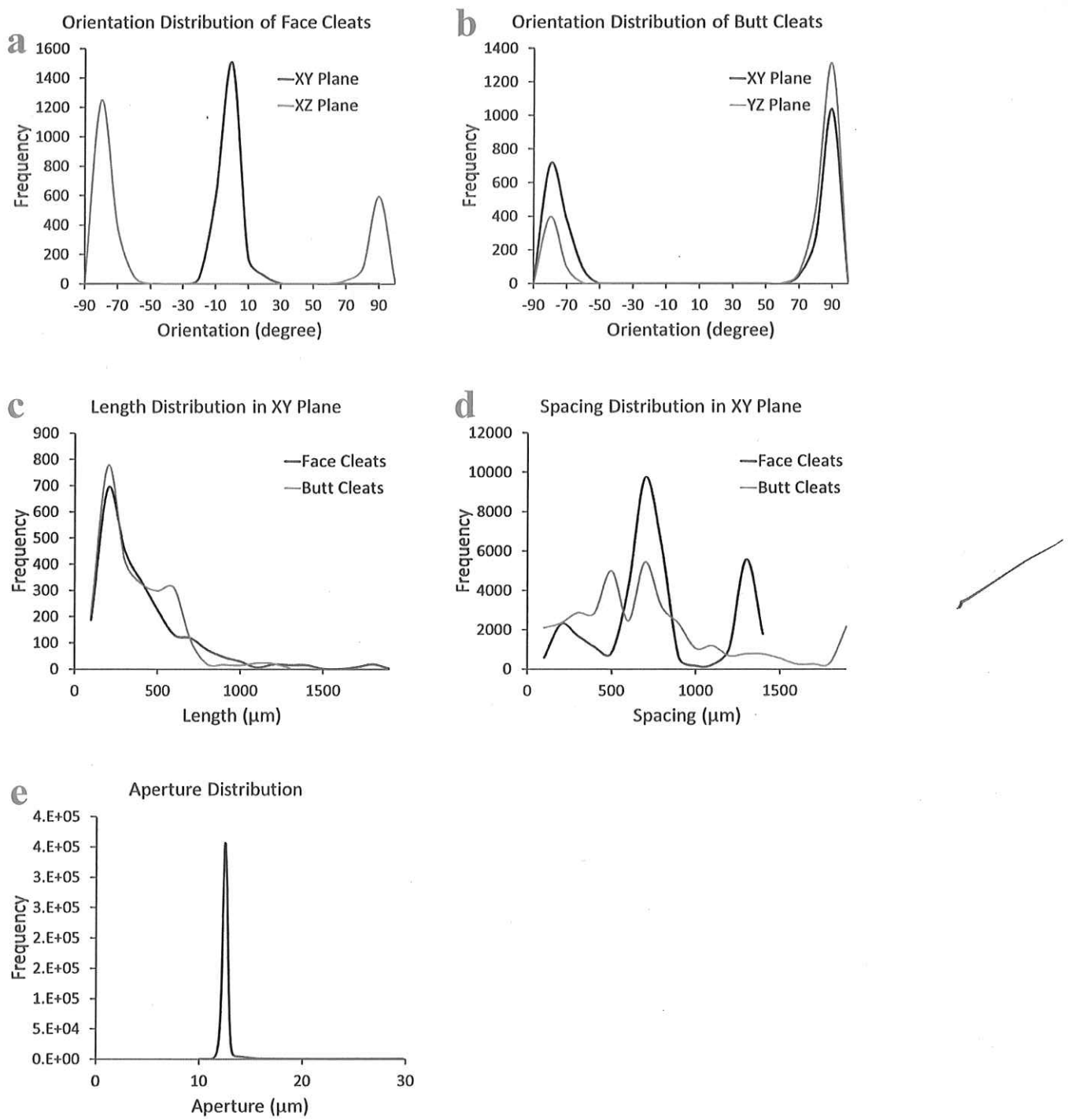


Figure 8: The following cleat statistics are measured: (a) orientation distributions of face cleats in XY plane and XZ plane; (b) orientation distributions of butt cleats in XY plane and YZ plane; (c) length distributions of face and butt cleats in XY plane; (d) spacing distributions of face and butt cleats in XY plane; and (e) the aperture size distribution.

Table 1: Summarised statistics data

Cleat Set	Cleat Parameters									
	Length (μm)		Azimuth (degree)		Dip (degree)		Spacing (μm)		Aperture (μm)	
	Avg.	Dev.	Avg.	Dev.	Avg.	Dev.	Avg.	Dev.	Avg.	Dev.
Face	354.4	281.2	173.9	6.6	94.4	7.6	820.9	475.6	12.6	0.26
Butt	324.5	207.6	91.2	9.7	85.7	7.8	784.1	566.4		

3.2 Flow Properties Analysis

3.2.1 Connectivity Analysis

To conduct a quantitative study of cleat connectivity, the construction of multiple DFN models can facilitate the estimation of fracture network connectivity (Mak 2015). To facilitate such an analysis, numerous DFN models are generated using a stochastic approach to assess the connectivity of the imaged coal sample. In this case, the input parameters with known distributions are orientation, length, spacing and aperture size. Each DFN model is a stochastic representation of the actual cleat network. This demonstrates that the corresponding connectivity results of different DFN scenarios are not identical. As such, a connectivity distribution is obtained.

In total 40 unique DFN realisations of the Moura coal sample with original sample dimensions ($960 \times 960 \times 170$) are generated stochastically by the Monte Carlo method. The connectivity of each realisation is measured and used to generate a connectivity probability distribution. To determine the number of realisations required to obtain the statistical average for connectivity, the relationship between the cumulative standard deviation and cumulative average of connectivity data versus the number of DFN realisations is plotted in Figure 9. After 15 realisations, both the averaged connectivity value and the standard deviation become relatively constant, i.e. the mean connectivity stabilises at 9 cm^{-2} and the standard deviation stabilises at 4.5 cm^{-2} . Therefore 15 realisations are sufficient to provide a stable probability distribution function (PDF) of cleat connectivity.

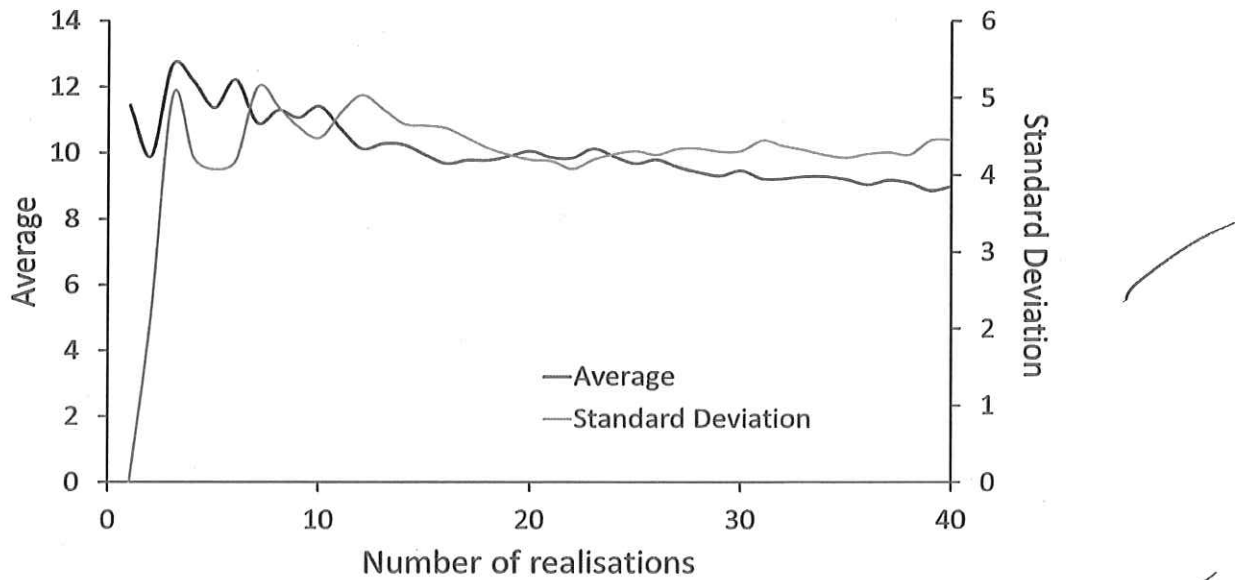


Figure 9: Cumulative standard deviation and cumulative average of connectivity versus the number of realisations. So 15 realisations are sufficient to give constant the connectivity distribution.

The connectivity histogram displayed in Figure 10 shows that the connectivity varies dramatically even with the same distributed geometric parameters. The most frequent connectivity is roughly around 10 cm^{-2} , which means that the cumulative intersection length in 1 cm^3 of coal is 10 cm. Also, as can be seen from the distribution, the connectivities of all DFN realisations are in the range of 2 cm^{-2} to 20 cm^{-2} . This implies that all of our mechanical DFN models have sufficient connectivity, while most of the previously reported Poisson DFN models (PM) have limited intersections, and are expected to be less favourable for fluid flow despite high fracture density (Alghalandis et al. 2011). Furthermore, the connectivity information is obtained before flow simulation and is extremely time efficient. Thus, only realisations with the most frequent connectivities are considered for simulation of flow and permeability calculations to save computational time.

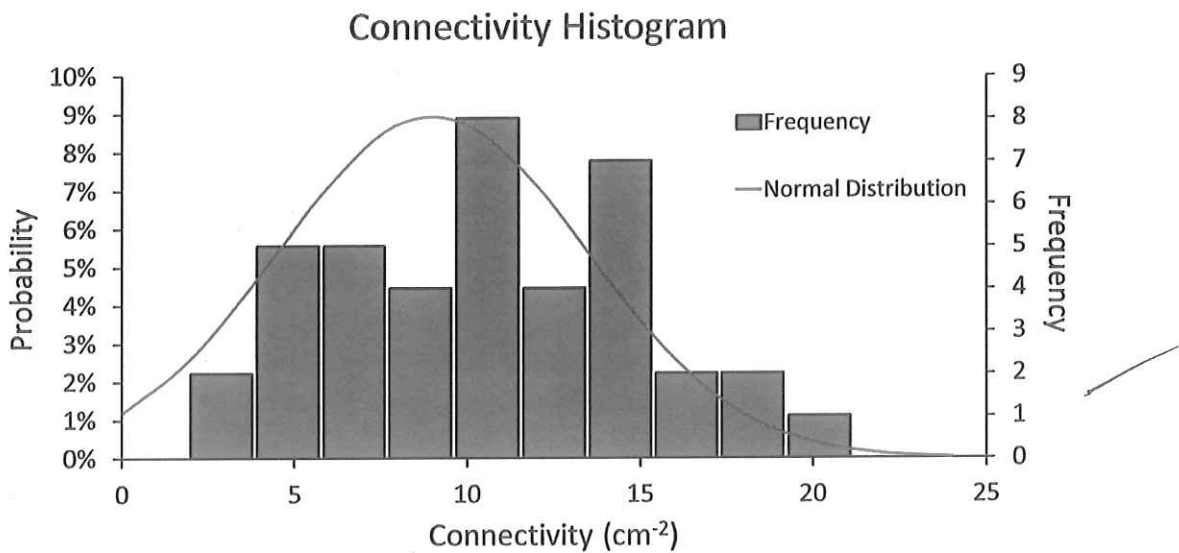


Figure 10: Analysed connectivity statistics, ranging from 2 to 20 cm⁻². The red line shows a Gaussian normal distribution match.

3.2.2 Permeability and Porosity Analysis

An analysis of permeability variation resulted from sample heterogeneity is presented. This comprises three steps: (1) constructing a number of DFN realisations; (2) subsampling the generated networks; (3) calculating the resulting permeability and porosity.

Eight realisations (Figure 11) with similar connectivities are selected from the total of 40 reconstructed DFN models, details of which are presented in Table 2. Each scenario has 15 sub-samples. Each sub-volume is centred on the centre of the image on the XY plane. And the scale variation of the domain size is only in the X and Y directions, increasing from 100×100×170 to 900×900×170 voxels.

Table 2: Parameters of 8 realisations

Realisation	Frequency	Intensity (cm ⁻¹)	Connectivity (cm ⁻²)	CPU (second)
1	132	24.39	11	1,406.41
2	111	25.61	8	1,213.90
3	115	25.12	18	1,372.68
4	120	24.88	11	1,131.51
5	104	24.88	8	1,235.74
6	123	26.10	16	1,330.47
7	121	23.90	14	1,263.86
8	107	24.88	9	1,381.29

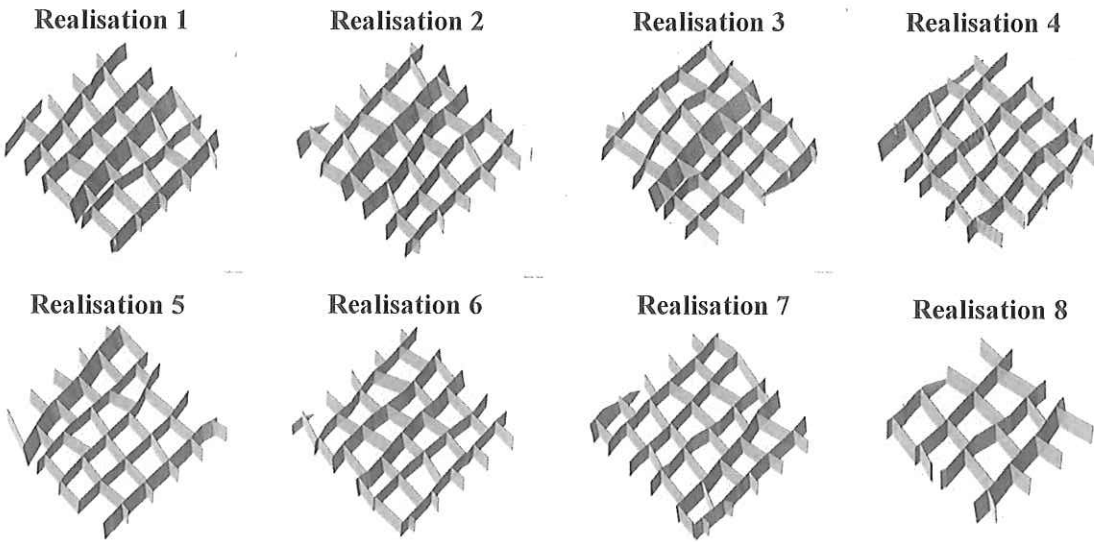


Figure 11: Eight selected realisations with a close degree of connectivity.

To investigate the multidirectional heterogeneity of permeability, x- and y-directional permeabilities are calculated for each sub-sample (k_x is normal to face cleats, and k_y is normal to butt cleats) and plotted in Figures 12 and 13. It is found that subsamples do not percolate in x-direction until the dimension is greater than $250 \times 250 \times 170$ voxels. However, in the y-direction, subsamples begin to percolate when the dimensions are greater than $180 \times 180 \times 170$ voxels. This is because face cleats are longer, offering lower percolation threshold. In addition, the variation of k_x gradually decreases with increasing dimension of the domain, while that of k_y does not reach a convergence. It emphasises that face cleat spacing has more profound effect on permeability than spacing of butt cleats. Consider the example of two subsamples from Realisation 6 in Figure 14, the number of cleats either in x or y direction increases with increased domain size. As a result, the x-directional permeability almost doubles, while the y-directional permeability presents only a slight rise. As can be seen, the face cleats are longer and increasing the size of the domain leads to introducing more pathways for fluid to percolate through. This is why k_y varies dramatically when more face cleats are introduced. Thus, face cleats play a more critical role in coal permeability compared with butt cleats, which demonstrates that the spacing of face cleats is more significant in terms of the permeability. From a macroscopic point of view, in coal reservoir exploitation, because of the dominance of face cleats over butt cleats on determining coal permeability, a particular well pattern should be developed to provide greater pressure drop. Commonly, wells developed for coal reservoirs have an elliptical drainage area, and highest pressure drop in the direction of face cleats, i.e. normal to butt cleats.

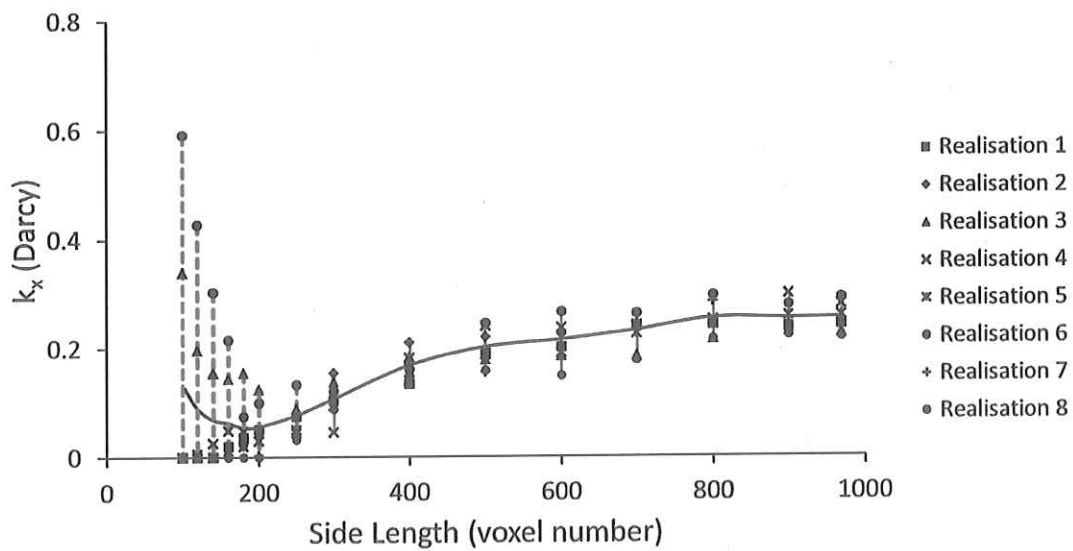


Figure 12: X-directional permeability versus domain dimension. All of the domains only have size variant in x and y directions, with the side length in z direction to be constantly 170 voxels. The effective directional permeability is normal to the face cleats. The x-directional average permeability becomes constant at around 0.25 Darcy when the domain size is greater than $800 \times 800 \times 170$ voxels.

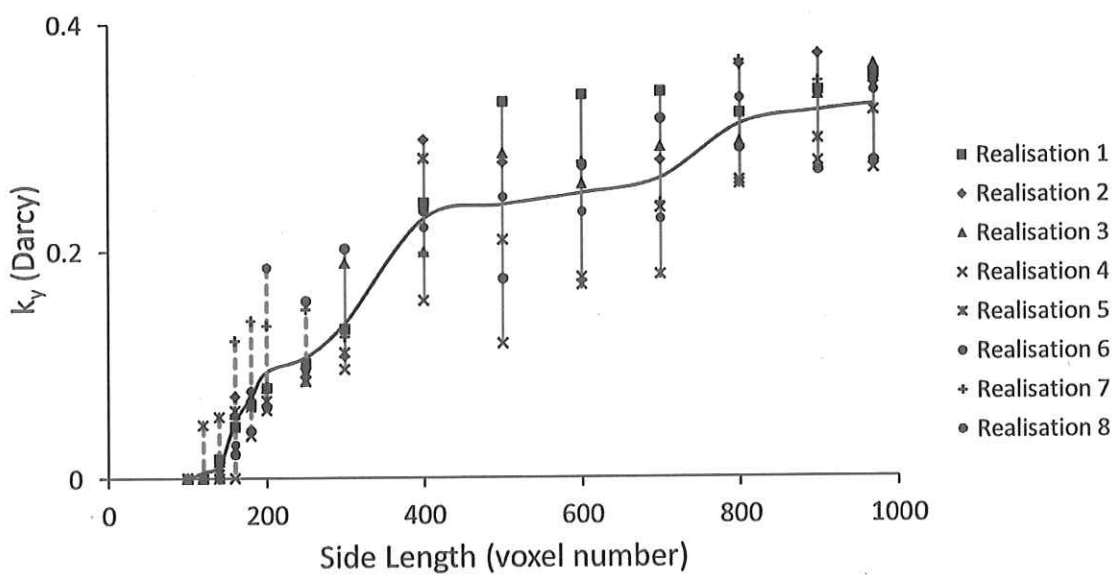


Figure 13: Y-directional permeability, normal to butt cleats, versus domain dimension. The y-directional average permeability increases significantly with increasing domain size, reaching a plateau when the size around $900 \times 900 \times 170$ voxels. The permeability variation at each size is more obvious than that of x-directional permeability.

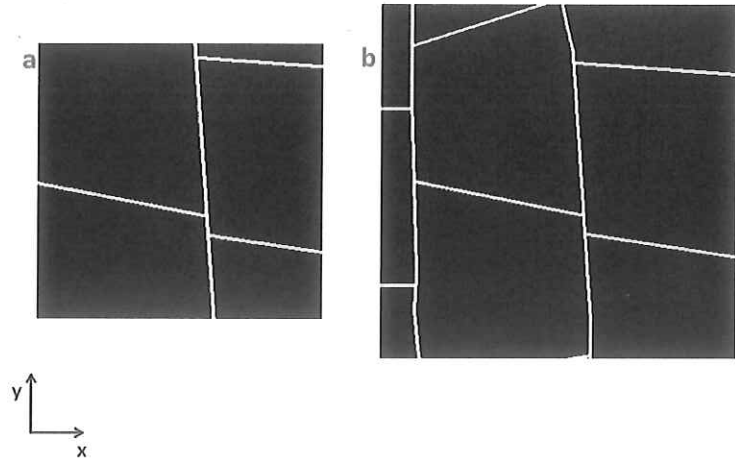


Figure 14: Two subsamples from the Realisation 6 with sizes of (a) $300 \times 300 \times 170$ and (b) $400 \times 400 \times 170$ voxels. X- and y-directional permeabilities of sample (a) are $0.1045D$ and $0.131D$ respectively, and those of sample (b) are $0.1345D$ and $0.242D$. Therefore, with the increase of domain size, the y-directional permeability almost doubles, while x-directional permeability presents only a slight rise. This indicates that face cleats play a more crucial role in the contribution of permeability.

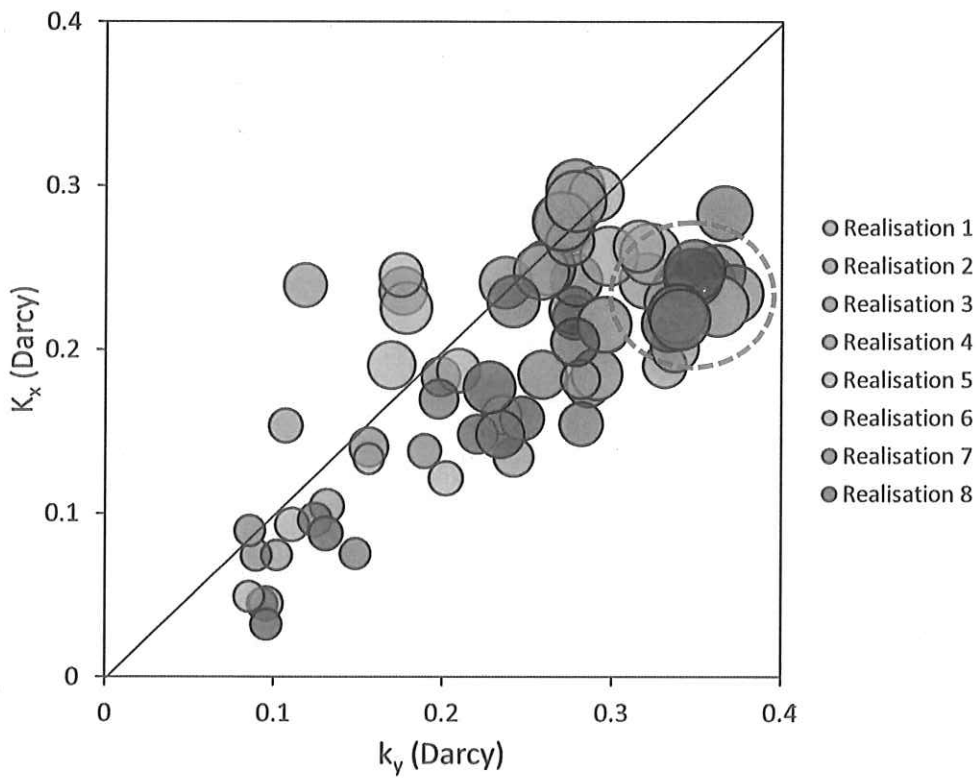


Figure 15: Comparison of directional permeabilities. The size of circles indicates the subsample size, i.e. larger circles mean larger subsamples. The majority of circles are distributed in the lower part, so this plug is more permeable in the direction of face cleats. Also, larger circles show an apparent overlap, meaning that the anisotropy is also scale-biased.

Figure 15 shows the directional permeability of all sub-samples. The size of the circles represents the subsample size (ranging from $100 \times 100 \times 170$ to $970 \times 970 \times 170$ voxels). For small sample volumes the circles are located around the straight line ($y = x$), implying that the coal sample is slightly anisotropic. However, as the sample size is increased the majority of points fall below the 1-to-1 line. As such, this plug is more permeable in the direction of face cleats, i.e. normal to butt cleats. Also, the larger circles show an apparent overlap, meaning that the anisotropy is scale-biased. In addition, the networks for face and butt cleats scale differently and the larger the domain size, the more anisotropic the sample is.

On the other hand, porosity of the coal plug presents a much smaller variation at each domain dimension (Figure 16). We observe a convergence when sub-volumes are larger than $500 \times 500 \times 170$ voxels, while that of k_x fluctuates until a size of $800 \times 800 \times 170$ voxels. This indicates that scaling has a stronger effect on permeability rather than porosity. This is in agreement with the measurements by Mostaghimi et al. (2013) even though their focus was on conventional reservoir rocks such as sandstones and carbonates. This is a consequence that permeability is dependent on more parameters (e.g. connectivity, percolation threshold, cleat size, aperture, spacing and etc.) in comparison with porosity. In addition, Ramandi et al (2016) showed that permeability of coal is not strongly affected by its porosity, highlighting the more profound importance of connectivity in coals and thus the importance of the presented connectivity and permeability analyses.

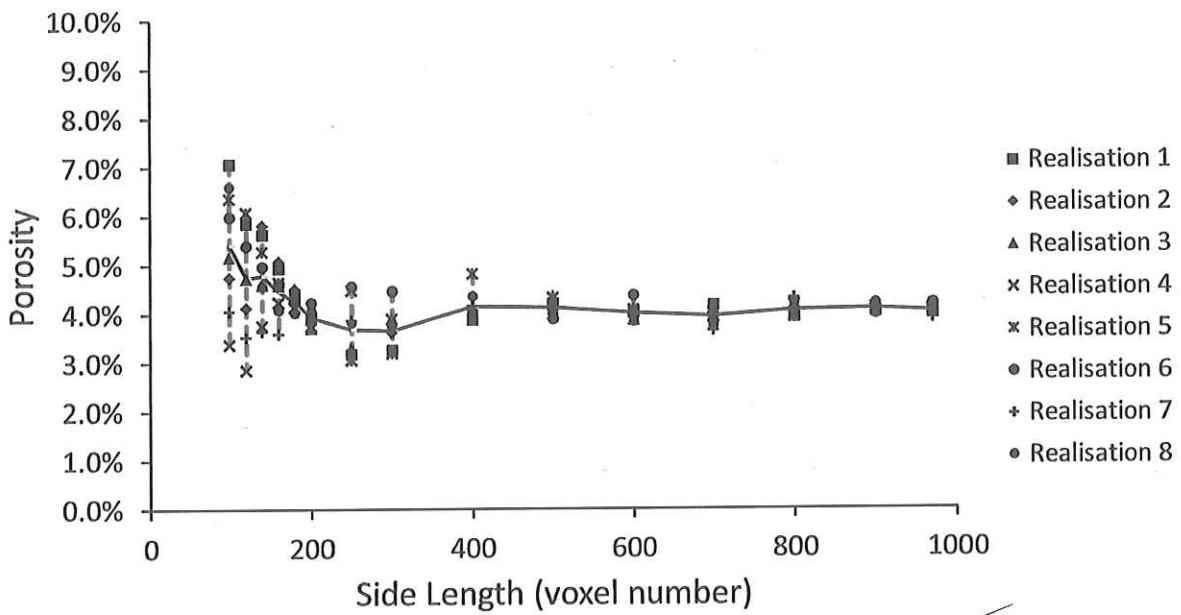


Figure 16: Porosity versus domain dimension. When the domain is larger than $500 \times 500 \times 170$ voxels, the porosity value is stabilised.

4 CONCLUSIONS

Statistics extraction from μ CT image analysis has been improved in terms of efficiency and accuracy. The presented quantitative imaging analysis is automatic without manual aid. Also, filtering fracture orientation was automatically realised, thereby contributing to better understanding of face cleats and butt cleat as two separate families. Cleat family classification facilitates the reliability of spacing and length statistics and provides new insights into coal permeability characterisation. Based on the extracted distributions, stochastic DFN realisations were generated mimicking the underlying cleat structure. By reconstructing DFN models with the same geometrical statistics and network patterns of real samples, significant properties, e.g. connectivity, permeability, porosity, can be quantified and the heterogeneity and anisotropy of coal can be evaluated. μ CT images of coal are challenging to segment correctly, which results in useless bottle-necked fracture structures and non-conductive cleat networks. However, the present DFN approach provides a fracture network that is favourable for direct numerical simulation. High-resolution μ CT images are also limited to the scanned sample size, while scanning larger samples reduces the image resolution and thus micro-cleats are lost. However, if the distributions are proven to be applicable for building larger models, the model domain can be extended for a given set of fracture statistics. The details of this will be the focus of a future paper.

However, there are some limitations in this work, which are recommended to be the focus of future studies:

- The aperture of each cleat is assumed to be constant, while real cleats have rough walls and variable opening widths. Applying some correction terms in calculating the aperture size of each cleat based on its surface roughness would be recommended.
- Aperture measurement currently cannot be based on different cleat families. So a global aperture distribution was used.
- DFN modelling in this work focused on bright coal, which has a more regular cleat pattern. For dull coal where the cleats are irregular, the method would require alteration.
- The models only reconstructed cleat networks in a thin section due to computational efficiency. However, the method can be applied to larger samples. Developing parallel algorithms, OpenMPI or MPI, are recommended to analyse larger coal samples.

REFERENCE

- Alghalandis, Y. F., C. Xu and P. A. Dowd (2011). A general framework for fracture intersection analysis: algorithms and practical applications. Australian Geothermal Energy Conference.
- Arns, C. H., F. Baugé, A. Limaye, A. Sakellariou, T. Senden, A. Sheppard, R. M. Sok, V. Pinczewski, S. Bakke and L. I. Berge (2005). "Pore scale characterization of carbonates using X-ray microtomography." Spe Journal **10**(04): 475-484.
- Baecher, G., N. Lanney and H. Einstein (1977). Statistical description of rock properties and sampling. The 18th US Symposium on Rock Mechanics (USRMS), American Rock Mechanics Association.
- Barenblatt, G., I. P. Zheltov and I. Kochina (1960). "Basic concepts in the theory of seepage of homogeneous liquids in fissured rocks [strata]." Journal of applied mathematics and mechanics **24**(5): 1286-1303.
- Bigun, J., T. Bigun and K. Nilsson (2004). "Recognition by symmetry derivatives and the generalized structure tensor." Pattern Analysis and Machine Intelligence, IEEE Transactions on **26**(12): 1590-1605.
- Blaskovich, F. T., G. M. Cain, F. Sonier, D. Waldren and S. J. Webb (1983). A Multicomponent Isothermal System for Efficient Reservoir Simulation. Middle East Oil Technical Conference and Exhibition. Manama, Society of Petroleum Engineers.
- Bonneau, F., V. Henrion, G. Caumon, P. Renard and J. Sausse (2013). "A methodology for pseudo-genetic stochastic modeling of discrete fracture networks." Computers & Geosciences **56**: 12-22.
- Bossie-Codreanu, D., K.-H. A. Wolf and R. Ephraim (2004). "A new characterization method for coal bed methane." Geologica Belgica **7**(3-4): 37-145.
- Botros, F. E., A. E. Hassan, D. M. Reeves and G. Pohll (2008). "On mapping fracture networks onto continuum." Water resources research **44**(8).
- Cacas, M., E. Ledoux, G. d. Marsily, B. Tillie, A. Barbreau, E. Durand, B. Feuga and P. Peaudecerf (1990). "Modeling fracture flow with a stochastic discrete fracture network: Calibration and validation: 1. The flow model." Water Resources Research **26**(3): 479-489.
- Caselles, V., R. Kimmel and G. Sapiro (1997). "Geodesic active contours." International journal of computer vision **22**(1): 61-79.
- Chen, S., Z. Wang, X. Shan and G. D. Doolen (1992). "Lattice Boltzmann computational fluid dynamics in three dimensions." Journal of Statistical Physics **68**(3): 379-400.
- Chen, S. H., X. M. Feng and S. Isam (2008). "Numerical estimation of REV and permeability tensor for fractured rock masses by composite element method." International journal for numerical and analytical methods in geomechanics **32**(12): 1459-1477.
- Correia, M., C. Maschio, D. J. Schiozer and M. Santos (2011). Upscaling Technique Applied to Naturally Fractured Carbonate Reservoirs. Brasil Offshore, Society of Petroleum Engineers.
- Deisman, N., D. M. Ivars, C. Darcel and R. J. Chalaturnyk (2010). "Empirical and numerical approaches for geomechanical characterization of coal seam reservoirs." International Journal of Coal Geology **82**(3): 204-212.
- Dershowitz, W. and H. Einstein (1988). "Characterizing rock joint geometry with joint system models." Rock Mechanics and Rock Engineering **21**(1): 21-51.
- Dershowitz, W., J. Hermanson, S. Follin and M. Mauldon (2000). Fracture intensity measures in 1-D, 2-D, and 3-D at Äspö, Sweden. 4th North American Rock Mechanics Symposium, American Rock Mechanics Association.
- Dershowitz, W., P. La Pointe and T. Doe (2004). Advances in discrete fracture network modeling. Proceedings of the US EPA/NGWA Fractured Rock Conference, Portland: 882-894.
- Dougherty, R. and K.-H. Kunzelmann (2007). "Computing local thickness of 3D structures with ImageJ." Microscopy and Microanalysis **13**(S02): 1678-1679.
- Elmo, D., S. Rogers, D. Stead and E. Eberhardt (2014). "Discrete Fracture Network approach to characterise rock mass fragmentation and implications for geomechanical upscaling." Mining Technology **123**(3): 149-161.

Erhel, J., J.-R. De Dreuzy and B. Poirriez (2009). "Flow simulation in three-dimensional discrete fracture networks." *SIAM Journal on Scientific Computing* **31**(4): 2688-2705.

Gamson, P. D., B. B. Beamish and D. P. Johnson (1993). "Coal microstructure and micropermeability and their effects on natural gas recovery." *Fuel* **72**(1): 87-99.

Gao, F., D. Stead and H. Kang (2014). "Numerical investigation of the scale effect and anisotropy in the strength and deformability of coal." *International Journal of Coal Geology* **136**: 25-37.

Gong, B. (2007). *Effective Models of Fractured Systems*. Doctor of Philosophy, Stanford University.

Gonzales, R. C. and R. E. Woods (1987). *Digital Image Processing*. MA, Addison & Wesley Publishing Company.

Gueguen, Y. and J. Dienes (1989). "Transport properties of rocks from statistics and percolation." *Mathematical geology* **21**(1): 1-13.

Hamawand, I., T. Yusaf and S. G. Hamawand (2013). "Coal seam gas and associated water: A review paper." *Renewable and Sustainable Energy Reviews* **22**: 550-560.

Hill, A. and G. Thomas (1985). A new approach for simulating complex fractured reservoirs. *Middle East Oil Technical Conference and Exhibition*, Society of Petroleum Engineers.

Hsieh, P. A., S. P. Neuman, G. K. Stiles and E. S. Simpson (1985). "Field Determination of the Three - Dimensional Hydraulic Conductivity Tensor of Anisotropic Media: 2. Methodology and Application to Fractured Rocks." *Water Resources Research* **21**(11): 1667-1676.

Jahne, B. (1993). *Spatio-Temporal Image Processing: Theory and Scientific Applications*, Springer-Verlag New York, Inc.

Johns, R. A., J. S. Steude, L. M. Castanier and P. V. Roberts (1993). "Nondestructive measurements of fracture aperture in crystalline rock cores using X ray computed tomography." *Journal of Geophysical Research: Solid Earth (1978–2012)* **98**(B2): 1889-1900.

Katsevich, A. (2002). "Theoretically Exact Filtered Backprojection-Type Inversion Algorithm for Spiral CT." *SIAM Journal on Applied Mathematics* **62**(6): 2012-2026.

Kazemi, H., L. Merrill Jr, K. Porterfield and P. Zeman (1976). "Numerical simulation of water-oil flow in naturally fractured reservoirs." *Society of Petroleum Engineers Journal* **16**(06): 317-326.

Ketcham, R. A., D. T. Slottke and J. M. Sharp (2010). "Three-dimensional measurement of fractures in heterogeneous materials using high-resolution X-ray computed tomography." *Geosphere* **6**(5): 499-514.

Lang, P., A. Paluszny and R. Zimmerman (2014). "Permeability tensor of three - dimensional fractured porous rock and a comparison to trace map predictions." *Journal of Geophysical Research: Solid Earth* **119**(8): 6288-6307.

Latham, S., T. Varslot and A. Sheppard (2008). "Image registration: enhancing and calibrating X-ray micro-CT imaging." *Proc. of the Soc. Core Analysts, Abu Dhabi, UAE*.

Laubach, S., R. Marrett, J. Olson and A. Scott (1998). "Characteristics and origins of coal cleat: a review." *International Journal of Coal Geology* **35**(1): 175-207.

Lee, T.-C., R. L. Kashyap and C.-N. Chu (1994). "Building skeleton models via 3-D medial surface/axis thinning algorithms." *CVGIP: Graph. Models Image Process.* **56**(6): 462-478.

Long, J. and P. A. Witherspoon (1985). "The relationship of the degree of interconnection to permeability in fracture networks." *Journal of Geophysical Research: Solid Earth (1978–2012)* **90**(B4): 3087-3098.

Lorig, L., C. Darcel, B. Damjanac, M. Pierce and D. Billaux (2015). "Application of discrete fracture networks in mining and civil geomechanics." *Mining Technology* **124**(4): 239-254.

Maffucci, R., S. Bigi, S. Corrado, A. Chiodi, L. Di Paolo, G. Giordano and C. Invernizzi (2015). "Quality assessment of reservoirs by means of outcrop data and "discrete fracture network" models: The case history of Rosario de La Frontera (NW Argentina) geothermal system." *Tectonophysics* **647–648**(0): 112-131.

Maillot, J., P. Davy, R. Le Goc, C. Darcel, J.-R. de Dreuzy and M. Stigsson (2014). Comparison between "Poissonian" and "mechanically-oriented" DFN models for the prediction of permeability and flow channeling.

Mak, S. W. (2015). Assessing fracture network connectivity of prefeasibility-level high temperature geothermal projects using discrete fracture network modelling at the Meager Creek site, southwestern British Columbia (NTS 092J). Geoscience BC Summary of Activities 2014, Report 2015-1: 123-128.

Marie Lefranc, S. F., Laurent Souche, Agnes Dubois (2012). Fractured basement reservoir characterization for fracture distribution, porosity and permeability prediction. AAPG International Conference and Exhibition, Singapore, Search and Discovery Article.

Martys, N. S. and H. Chen (1996). "Simulation of multicomponent fluids in complex three-dimensional geometries by the lattice Boltzmann method." Physical Review E 53(1): 743-750.

Mazumder, S., K.-H. Wolf, K. Elewaut and R. Ephraim (2006). "Application of X-ray computed tomography for analyzing cleat spacing and cleat aperture in coal samples." International Journal of Coal Geology 68(3): 205-222.

Mostaghimi, P., R. T. Armstrong, A. Gerami, M. E. Warkaini, H. L. Ramandi and V. Pinczewski (2015a). Micro-CT imaging and microfluidics for understanding flow in coal seam reservoirs. Proc. of International Symposium of the Society of Core Analysts, Newfoundland, Canada.

Mostaghimi, P., M. J. Blunt and B. Bijeljic (2013). "Computations of absolute permeability on micro-CT images." Mathematical Geosciences 45(1): 103-125.

Mostaghimi, P., Tollit, B. S., Neethling, S. J., Gorman, G. J. and Pain, C. C. (2014). "A control volume finite element method for adaptive mesh simulation of flow in heap leaching." Journal of Engineering Mathematics, 87(1), 111-121.

Mostaghimi, P. and H. Mahani (2010). "A quantitative and qualitative comparison of coarse-grid-generation techniques for modeling fluid displacement in heterogeneous porous media." SPE Reservoir Evaluation & Engineering 13(01): 24-36.

Mostaghimi, P., J. R. Percival, D. Pavlidis, R. J. Ferrier, J. L. Gomes, G. J. Gorman, M. D. Jackson, S. J. Neethling and C. C. Pain (2015b). "Anisotropic mesh adaptivity and control volume finite element methods for numerical simulation of multiphase flow in porous media." Mathematical Geosciences 47(4): 417-440.

Muralidharan, V., D. Chakravarthy, E. Putra and D. Schechter (2004). Investigating fracture aperture distributions under various stress conditions using X-ray CT scanner. Canadian International Petroleum Conference, Petroleum Society of Canada.

Norouzi Apourvari, S. and C. H. Arns (2016). "Image-based relative permeability upscaling from the pore scale." Advances in Water Resources, In press.

Oda, M. (1985). "Permeability tensor for discontinuous rock masses." Geotechnique 35(4): 483-495.

Pan, J.-B., C.-C. Lee, C.-H. Lee, H.-F. Yeh and H.-I. Lin (2010). "Application of fracture network model with crack permeability tensor on flow and transport in fractured rock." Engineering Geology 116(1): 166-177.

Parashar, R. and D. M. Reeves (2011). "Computation of flow and transport in fracture networks on a continuum grid." Proceedings of MODFLOW and MORE: 752-756.

Pattison, C., C. Fielding, R. McWatters and L. Hamilton (1996). "Nature and origin of fractures in Permian coals from the Bowen Basin, Queensland, Australia." Geological Society, London, Special Publications 109(1): 133-150.

Ramandi, H. L., P. Mostaghimi, R. T. Armstrong, M. Saadatfar and W. V. Pinczewski (2016). "Porosity and permeability characterization of coal: a micro-computed tomography study." International Journal of Coal Geology 154–155: 57-68.

Robertson, A. (1970). The interpretation of geological factors for use in slope theory. Planning Open Pit Mines, Proceedings, Johannesburg: 55-71.

Robinson, P. (1983). "Connectivity of fracture systems-a percolation theory approach." Journal of Physics A: Mathematical and General 16(3): 605.

Rodrigues, C., C. Laiginhas, M. Fernandes, M. L. de Sousa and M. Dinis (2014). "The coal cleat system: A new approach to its study." Journal of Rock Mechanics and Geotechnical Engineering 6(3): 208-218.

Schlüter, S., A. Sheppard, K. Brown and D. Wildenschild (2014). "Image processing of multiphase images obtained via X-ray microtomography: A review." Water Resources Research **50**(4): 3615-3639.

Scholtès, L., F.-V. Donzé and M. Khanal (2011). "Scale effects on strength of geomaterials, case study: coal." Journal of the Mechanics and Physics of Solids **59**(5): 1131-1146.

Seidle, J. (2011). Fundamentals of Coalbed Methane Reservoir Engineering, PennWell Corporation.

Sheppard, A., S. Latham, J. Middleton, A. Kingston, G. Myers, T. Varslot, A. Fogden, T. Sawkins, R. Cruikshank, M. Saadatfar, N. Francois, C. Arns and T. Senden (2014). "Techniques in helical scanning, dynamic imaging and image segmentation for improved quantitative analysis with X-ray micro-CT." Nuclear Instruments and Methods in Physics Research Section B: Beam Interactions with Materials and Atoms **324**: 49-56.

Sheppard, A. P., R. M. Sok and H. Averdunk (2004). "Techniques for image enhancement and segmentation of tomographic images of porous materials." Physica A: Statistical Mechanics and its Applications **339**(1-2): 145-151.

Svensson, U. (2001). "A continuum representation of fracture networks. Part I: Method and basic test cases." Journal of Hydrology **250**(1): 170-186.

van der Most, M. (2008). The analysis of directional permeability of fractured reservoirs: A case study from the Tata area, Morocco, MS thesis, Delft University of Technology, Delft, The Netherlands.

Vandersteen, K., B. Busselen, K. Van Den Abeele and J. Carmeliet (2003). "Quantitative characterization of fracture apertures using microfocus computed tomography." Geological Society, London, Special Publications **215**(1): 61-68.

Vincent, L. and P. Soille (1991). "Watersheds in Digital Spaces - an Efficient Algorithm Based on Immersion Simulations." Ieee Transactions on Pattern Analysis and Machine Intelligence **13**(6): 583-598.

Vohralík, M., J. Maryška and O. Severýn (2007). "Mixed and nonconforming finite element methods on a system of polygons." Applied numerical mathematics **57**(2): 176-193.

Voorn, M., U. Exner, A. Barnhoorn, P. Baud and T. Reuschlé (2014). "Porosity, permeability and 3D fracture network characterisation of dolomite reservoir rock samples." Journal of Petroleum Science and Engineering.

Warren, J. and P. J. Root (1963). The behavior of naturally fractured reservoirs, SPE Journal.

Wolf, K.-H. A., D. B. Codreanu, R. Ephraim and N. Siemons (2004). "Analysing cleat angles in coal seams using image analysis techniques on artificial drilling cuttings and prepared coal blocks." Geol. Belg **7**(3-4): 105-114.

Wolf, K.-H. A. A., F. van Bergen, R. Ephraim and H. Pagnier (2008). "Determination of the cleat angle distribution of the RECOPOL coal seams, using CT-scans and image analysis on drilling cuttings and coal blocks." International Journal of Coal Geology **73**(3-4): 259-272.

Yang, T., P. Jia, W. Shi, P. Wang, H. Liu and Q. Yu (2014). "Seepage-stress coupled analysis on anisotropic characteristics of the fractured rock mass around roadway." Tunnelling and Underground Space Technology **43**: 11-19.

Yuen, M., S. Tan and K. Hung (1991). "A hierarchical approach to automatic finite element mesh generation." International journal for numerical methods in engineering **32**(3): 501-525.

